SSRG International Journal of Electrical and Electronics Engineering
ISSN: 2348-8379/ https://doi.org/10.14445/23488379/IJEEE-V13I9P102

Volume 13 Issue 9, 17-32, September 2026

Original Article

A Planar Multiport Multi-Circular Patch MIMO Antenna on Flexible Substrate with Defected Ground Structure for Sub-6 GHz

Fahmida Hossain[1], Mohd Khanapiah Bin Nor[1], Azlan Abd Aziz[2], Muhammad Ibn Ibrahimy[3], A.K.M. Zakir Hossain[1]*

[1]*Center for Telecommunication Research & Innovation, Fakulti Teknologi Dan Kejuruteraan Elektronik Dan Komputer, Universiti Teknikal Malaysia Melaka, Jalan Hang Tuah Jaya, Durian Tunggal, Melaka 76100, Malaysia.*
[2]*Centre of Wireless Technologies, Faculty of Engineering and Technology, Multimedia University, Melaka, Malaysia.*
[3]*Depertment of Electrical and Computer Engineering, Faculty of Engineering, International Islamic University Malaysia, Gombak, Malaysia.*

[1*]*Corresponding Author : zakir@utem.edu.my*

Received: 13 May 2026 Revised: 05 August 2026 Accepted: 27 August 2026 Published: 26 September 2026

Abstract - *In this proposed work, a flexible planar six-port Multiple-Input Multiple-Output (MIMO) microstrip antenna is presented that is intended for sub-6 GHz Fifth Generation (5G), wearable, and biomedical wireless applications. The antenna employs a multi-circular radiating patch topology. It is integrated with a Partial Ground Plane (PGP) and a Defected Ground Structure (DGS) techniques to achieve wideband impedance matching, reduced mutual coupling, and improved diversity characteristics. The single antenna element occupies a small space of 38.40 × 24 × 0.508 mm³, whereas the complete six-port configuration is arranged on a 165 × 76 mm² flexible Kapton platform corresponding to the dimensions of a 6.67-inch smartphone. The practical measurements demonstrate a wide bandwidth of 3.0-6.6 GHz, which includes all available sub-6 GHz 5G mid-band frequencies. The measured inter-port isolation remains greater than 35 dB and reaches approximately 58 dB for selected port combinations. The Envelope Correlation Coefficient (ECC) is maintained below 0.5, with a minimum of* 1.15×10^{-5} *while the Diversity Gain (DG) remains close to 10 dB. The Mean Effective Gain (MEG) is approximately 3 dB for all ports, with inter-port differences close to 0 dB. Practical line-of-sight measurements produce received-power levels ranging from -37.24 to -22.92 dBm. The antenna also preserves stable operation during on-body placement and mechanical bending. Moreover, the maximum specific absorption rate values are 0.775 W/kg averaged over 1 g of tissue and 0.335 W/kg averaged over 10 g, remaining within the applicable exposure limits.*

Keywords - *MIMO, Flexible antenna, Defected ground structure, Sub-6 GHz, Kapton substrate, SAR.*

1. Introduction

The technology shift in the field of wireless digital communication is everchanging and since the adoption of 5G in this filed, the researchers have intensified the research on compact, high-performance antenna systems suitable for smartphones and other mobile/wireless platforms [1, 2]. In the current era of MIMO technology, the antenna arrays are well known to boost the channel capacity within given bandwidth constrains, reliability, spectral efficiency, data rate and throughput. However, the design of MIMO arrays for sub-6 GHz mobile applications presents persistent challenges, particularly with respect to mutual coupling, isolation, and efficiency when multiple elements are integrated into limited device form factors. A broad range of antenna structures, such as patch, monopole, slot, and their variations, have been explored in recent studies to address these issues [3]. It is important to address the existing design strategies, highlighting their operating principles, performance trade-offs, and limitations, in order to identify the gaps that motivate the proposed planar MIMO array design [4].

2. Literature Review

One of the significant works is presented in [5], where the authors have proposed a four-port MIMO array that works in dual-band employing compact self-decoupled radiators. The operating range is between 3.4-3.6 GHz and 4.8-5.0 GHz by positioning adjacent antenna pairs close together and allowing them to share a common grounding branch to achieve inherent decoupling. Consequently, the design provided isolation around -17.5 dB and -20dB for the lower and upper 5G mid band, respectively. The value of the ECC is <0.14 and <0.12, while the CCL is 15.8-16.8 b/s/Hz and 15.8-18 b/s/Hz for the two bands, respectively. Despite these strengths, the total efficiency remained limited to about 50% also no SAR compatibility results are presented. Moreover, [6] further investigated a single-sided design in which the antenna was mounted on an FR4 substrate along the edge of the Ground Plane (GP). This design is covering a dual band of 1.8-1.88 GHz (80 MHz bandwidth) and 3.4-3.6 GHz (200 MHz bandwidth) bands.

Composite capacitors were incorporated to realize a frequency-selective dual-band decoupling scheme, allowing the coupling response in each operating band to be controlled independently. The proposed design accomplished a S_{11} value of as low as -14 dB and -18 dB in the lower and upper band,s, respectively. The antenna also corresponding a good ECC values of 0.046 and 0.064. Its Radiation Efficiency (RE) ranged from 62% to 66% and from 50% to 62% in the lower and the upper band respectively. Nevertheless, the reported isolation levels of only 13 dB and 9 dB across the respective operating bandwidths remained below the commonly adopted 15 dB isolation criterion for MIMO antennas [7]. The use of parasitic strips to improve isolation in MIMO systems is proposed by [8, 9]. Furthermore, in [10], the authors extended this approach by presenting an eight-element MIMO structure for 5G smartphones, arranged as four antenna pairs along the device side frames. These designs employed wideband decoupled dual-antenna pairs based on characteristic mode theory, enabling full coverage of the 5 GHz spectrum and the n77/n78/n79 bands used in wireless local area networks. Parasitic strips were combined with defective ground structures to achieve broadband operation and enhanced isolation. This configuration maintained more than 15 dB of isolation across all port combinations. It also exhibited S_{11}below -32 dB, an ECC lower than 0.11, and a channel capacity loss of 41.3 b/s/Hz, while its total efficiency varied between 47% and 78%. Reference [11] subsequently introduced a four-port dual-band array covering 3.4-3.6 GHz and 4.8-5.0 GHz.

Each radiator combined rectangular parasitic, L-shaped, and modified Z-shaped conductive sections. The elements were positioned along the two longitudinal edges of the handset chassis, leaving sufficient space for the integration of legacy 2G, 3G, and 4G antennas. The reported isolation exceeded 16.5 dB, whereas the total efficiencies were 85% and 82% in the lower and upper bands, respectively. Corresponding realized gains of 4.7 and 5 dBi were obtained, with the ECC remaining below 0.01. To overcome bandwidth restrictions, the work in [12] integrated a four-element wideband MIMO arrangement directly with the metallic frame of a 5G smartphone, which the authors reported as the first highly integrated implementation of this type.

Self-isolation offers another way to avoid explicit decoupling hardware. The authors in [13] built a ten-element array from printed shorted loop elements operating in the half-wavelength mode, each occupying only 6 × 6.5 mm² and excited by a small capacitive flag-shaped strip, with inward meandering forming an internal loop that sets the resonance at 3.5 GHz. The measured band covers 3.4-3.6 GHz with a matching better than −10 dB, total efficiency between 65% and 78%, and peak gain from 4.2 to 5.9 dBi. Worst-case port isolation is 10 dB, obtained without neutralization lines, parasitic elements or slots, and the ECC stays below 0.055 with a channel capacity near 54.3 b/s/Hz. Standalone SAR was computed for each element against a hand phantom and stayed inside the 1.6 W/kg and 2 W/kg limits. The trade-off is bandwidth: the design covers only a 200 MHz slice at 3.5 GHz, and its isolation is the lowest among the works surveyed here.

A different route to broadband coverage was taken by Chen and Su [14], who placed an eight-port array in the four corners of a metal-framed handset rather than along its side edges, freeing a substantial amount of PCB area. Each antenna element is an open-slot structure, and each element is excited by a coupling shape called a T-shaped structure connected to a 50 Ω microstrip Transmission Line (TL), and measures only 12.25 × 2.5 × 7 mm³. A wide slot combined with a neutral line handles the coupling between adjacent elements. The array covers 3.3-6 GHz, spanning n77, n78, n79 and the 5 GHz WLAN band. The proposed design features decent isolation around 12 dB, peak realized gain between 2 and 5.28 dBi inside the working bandwidth. Additionally, it has a Total Efficiency (TE) from 37% to 71%, the ECC maintains below 0.34 throughout the entire band, and the in-band channel capacity is exhibited from 33 to 41 b/s/Hz. Two points qualify the result: the bandwidth is defined on a 6 dB criterion rather than the 10 dB one used in most of the works surveyed here, and no SAR analysis is reported.

Flexible and conformal implementations form a smaller but faster-growing branch of this literature, and they are the closest point of comparison for the present work. John et al. [15] built a four-element wideband MIMO antenna on a 0.25 mm polyethylene terephthalate film measuring 65 × 56 mm², in which a neutralization line in the radiator was combined with a defected ground structure to form a hybrid decoupling network, with characteristic mode analysis used to guide the design evolution. The measured band ran from 3.55 to 5.3 GHz with a peak gain of 4.9 dBi and isolation better than 24 dB, and the diversity figures were strong: ECC below 0.001, diversity gain above 9.99, and channel capacity loss under 0.3 b/s/Hz. SAR was reported as 0.745 W/kg for 1 g of tissue and 0.326 W/kg for 10 g. The coverage, however, stops well short of the upper half of the sub-6 GHz allocation, and the array is limited to four ports.

A textile route was taken by [16], where the authors have printed a two-port irregular octagonal patch with a parasitic strip on jeans fabric of 1 mm thickness and effective permittivity 1.6, over a 40 × 50 mm footprint. Slots in the partial ground and in the parasitic strip were used together to improve matching and reduce coupling. Measurement gave a band of 4.35-7 GHz against a simulated 3.6-7 GHz, with 28.5 dB of measured isolation and a peak gain of 6.74 dB. The gap between the simulated and measured lower band edge shows how sensitive fabric-based designs are to substrate tolerance. Neither SAR nor any link-level measurement was reported.Scaling to a higher port count on a flexible platform was addressed by Judice et al. [17]. Their octa-port design uses an offset-tapered feed with etched circular slots over a 0.254 mm laminate of permittivity 2.33, occupying 2975 mm², with the substrate micromachined at the centre to suppress surface-wave coupling. Isolation exceeds 20 dB, ECC stays below 0.001, and diversity gain approaches 10 dB. A conformal study at bend angles of 0°, 15°, 30°, and 45° showed no shift in either operating band, SAR remained under the 1.6 W/kg limit, and the measured peak gain reached 5.95 dBi at better than 80% efficiency. The usable sub-6 GHz coverage is nevertheless confined to a 400 MHz slice around 3.5 GHz. Table 1 comprises the summary of the discussion.

Table 1. Comparison of performance between existing designs

Citation	Band	Element	Isolation	SAR	LOS Test
	GHz		dB	W/Kg	Yes/No
[5]	3.3-6.0	8	> -12.1	na	No
[6]	1.8-1.9, 3.4-3.6	4	na	na	No
[8]	3.4-3.6 4.8-5.0	4	> -17.5	na	No
[10]	n77/n78/n79	8	> -15	na	No
[11]	3.4-3.6 4.8-5.0	4	> -16.5	na	No
[12]	3.3-5.0	4	> -10	na	No
[13]	3.4-3.6	10	> -10	within limits	No
[14]	3.3-6.0	8	> -12	na	No
[15]	3.5-5.3	4	> -24	0.75	No
[16]	4.35-7.0	2	> -28	na	No
[17]	3.5-3.9	8	>-20	1.6	No
Our Design	3.0-6.6	6	> - 35	0.119	Yes

***El. = element, Is = isolation, wl = within limits**

Table 1 makes the pattern visible. Reported isolation clusters between 10 and 24 dB, with a single measured outlier at 28.5 dB, and the designs reaching the upper end of that range do so over narrow or split bands rather than continuous ones. Three of the surveyed works use flexible substrates; among them, the widest measured continuous coverage is 4.35-7 GHz, and the sub-6 GHz portion of that is partial. SAR appears in three entries out of ten. Not one reports a link-level received-power measurement, so the transition from anechoic characterization to a working radio link is left unverified throughout.

The design presented here is positioned against precisely that combination: a single uninterrupted 3.0-6.6 GHz band on a flexible substrate, isolation beyond 35 dB across every port pair, port-resolved SAR, and LOS verification in flat, bent, and on-body states.

3. Synthesis of Single Antenna and MIMO

3.1. Single Element Design

The design steps of the proposed Single-Element Antenna (SEA) are illustrated in Figure 1. In the initial stage - S1, a single circular radiating patch with a radius of 5.2 mm is fed by a 50 Ω microstrip Transmission Line (TL) that is 22.48 mm in length and 1.93 mm in width. Equations (1) and (2) are used to determine the radius of the circular patch. This basic configuration is placed over a Full Ground Plane (FGP) covering the entire backside of the substrate, which serves as a conventional baseline design. The FGP often restricts the impedance bandwidth due to strong electromagnetic reflection and leads to narrowband responses. To address this limitation, the Second stage (S2) introduces a PGP by truncating the ground that is 19.70 mm of the lower half, especially under the radiating patch area. In the Third stage (S3), DGS is used at the top centre of the PGP.

These specific modifications unlock the improvement of the impedance matching and the extension of the working bandwidth, which is necessary for wideband performance. Moving into the Fourth stage - S4, two additional identical circular patches are symmetrically included adjacent to the original patch, which creates a three-patch copper trace layout. The inclusion of these co-radiating elements not only increases the effective aperture of the proposed antenna overall but also permits the excitation of multiple resonant modes, which results in better impedance bandwidth, higher gain, and more uniform radiation pattern coverage. In the Final (Fifth stage - S5) and most optimized design stage, two more identical circular patches are added, finishing with a five-circled structure, where all circular strip patches maintain the same 5.2 mm radius. This even proportioned multi-circular arrangement allows for constructive accumulation of the induced surface currents and a balanced field distribution, further improving the gain stability, bandwidth, and the radiation symmetry.

Figure 2 (a) comprises the simulated layout of the proposed design. By using the full wave 3-D electromagnetic simulator CST MWS 2025, the simulation is performed for this design. The stage-by-stage results are presented in the results and discussion section.

$$r = \frac{F}{\left\{1+\frac{2h}{\pi \varepsilon_r F}\left[ln\left(\frac{\pi F}{2h}\right)+1.7726\right]\right\}^{\frac{1}{2}}} \quad (1)$$

$$F = \frac{8.791 \times 10^9}{f_c\sqrt{\varepsilon_r}} \quad (2)$$

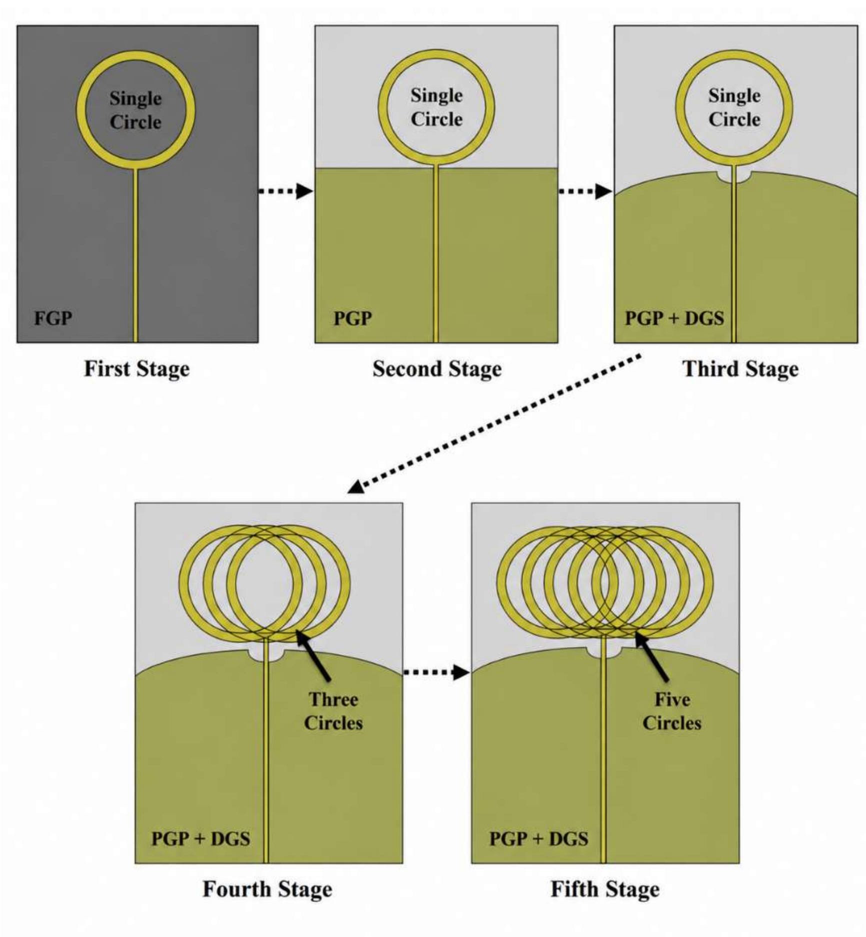

Fig. 1 Stages of the proposed SEA design

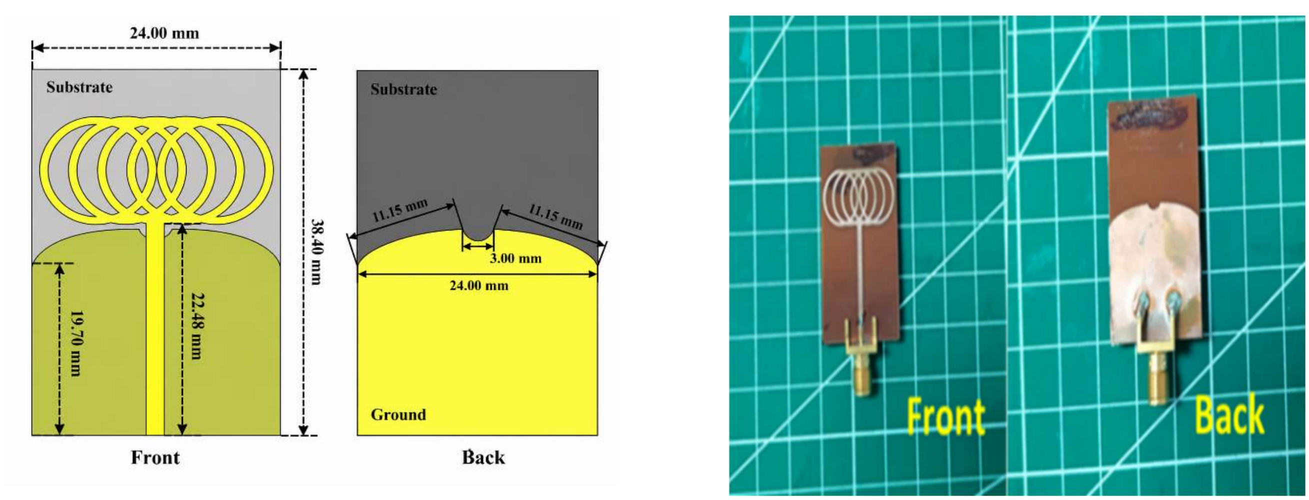

(a) **(b)**

Fig. 2 (a) Final optimized structure of the SEA and (b) The fabricated prototype on Kapton substrate.

After confirmation from the simulation, the proposed SEA has been fabricated by realizing it on the Kapton substrate using the etching process. The fabricated front and back view layout of the final SEA design from the CST workspace is described in Figure 2(b). The microstrip TL width is 0.84 mm, with the compact overall dimensions of 38.40 × 24 × 0.508 mm^3. In the simulation layout from the CST MWS 2025 workspace (Figure 2(a)), the yellow colour denotes the radiating patch and ground plane, while the grey colour indicates the flexible substrate material. In the fabricated prototype, the semicircular slot with a width of 24.00 mm is etched at the top centre of the patch, along with a central notch of 3.00 mm. The curved edges stretch 11.15 mm long symmetrically on both sides, helping to minimize mutual coupling and enhance impedance matching. This slotted and flexible design significantly contributes to increased isolation, broader bandwidth, and ECC, making it suitable for MIMO systems in modern wearable and wireless applications.

3.2. MIMO Antenna Array Design

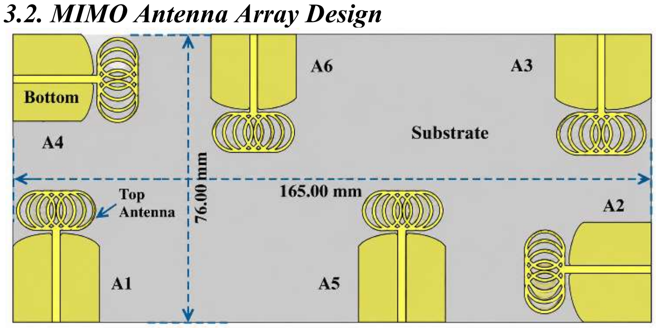

(a)

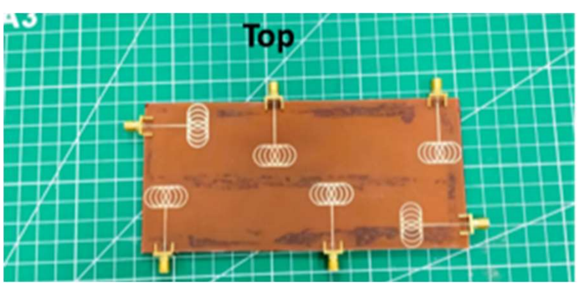

(b)

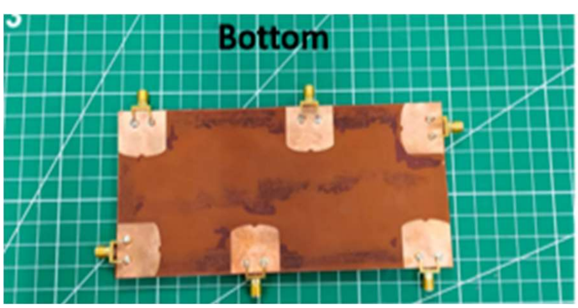

(c)

Fig. 3 (a) Final optimized structure of the 6×6 MIMO, and (b) and (c) are the top and bottom side of the prototype realized on Kapton substrate, respectively.

Figure 3 presents both the numerical model and the fabricated prototype of the six-port MIMO antenna. The final proposed antenna array occupies a $165 \times 76\ \text{mm}^2$ flexible platform, selected to approximate the footprint of a smartphone with a 6.67-inch display. Polarization diversity is introduced by orienting neighboring radiators at 90^0 relative to one another.

The antenna elements are identified as A1-A4 in the four-port configuration and A1-A6 in the six-port configuration. For the six-port arrangement, elements A5 and A6 are positioned on the opposite side of the board, while the separations between A1-A5 and A3-A6 are both 84 mm. The final configuration was subsequently evaluated in the presence of hand and head phantoms to examine user-proximity effects and assess its SAR characteristics.

3.3. Measurement Setups

Figure 4 reveals a different measurement setup to validate the design in different scenarios. First, the SEA and the MIMO are validated by the S-parameter analysis using the Vector Network Analyser (VNA). The setup is shown in Figure 4 (a) and 4 (b). Afterward, the antenna is placed inside an anechoic chamber to measure the far-field radiation pattern (illustrated in Figures 4 (c) and 4 (d)).

The proposed SEA and MIMO configurations are validated using the Line-of-Sight (LOS) setups shown in Figure 4 (e) and 4 (f), respectively, with a radiated/transmitted power of -10dBm. Lastly, the MIMO antenna is tested under various bending conditions with the same transmitted power. Figure 4 (g) depicts the MIMO antenna attached to a human arm; furthermore, bending performance is validated using a plastic bottle with a 50 mm radius.

All results are presented, analysed, and discussed in detail in the following section. Additional MIMO performance metrics, such as the ECC, DG, and MEG, are determined using measured S-parameters. Finally, the biocompatibility of the proposed antenna is validated by calculating port-by-port Specific Absorption Rate (SAR) values in CST MWS 2025, utilizing Equations (3)-(6) [18, 19].

$$SAR = \frac{\sigma |E|^2}{\rho} \quad (3)$$

$$\text{ECCij} = \frac{|S*_{ii}S_{ij}+S*_{ji}S_{jj}|^2}{(1-|S_{ii}|^2-|S_{ij}|^2)+(1-|S_{ji}|^2-|S_{jj}|^2)} \quad (4)$$

$$\text{DGij} = 10 \times \sqrt{1 - (\text{ECC}_{ij})^2} \quad (5)$$

$$\text{MEG}_i = 0.5(1 - \sum_{j=1}^{N} |S_{ij}|^2) \quad (6)$$

(a) S-parameter Measurement (SEA)

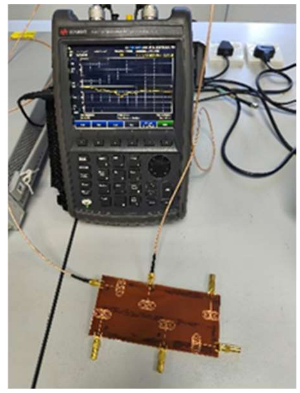

(b) S-parameter Measurement MIMO

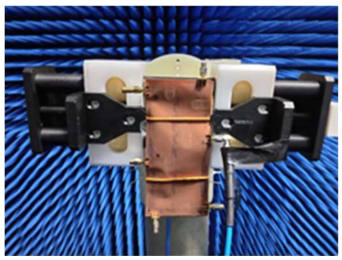

(c) Farfield measurement

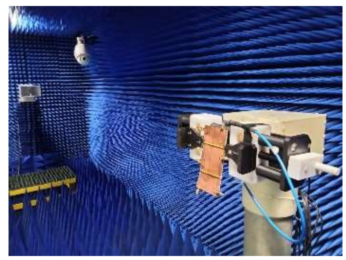

(d) Farfield measurement

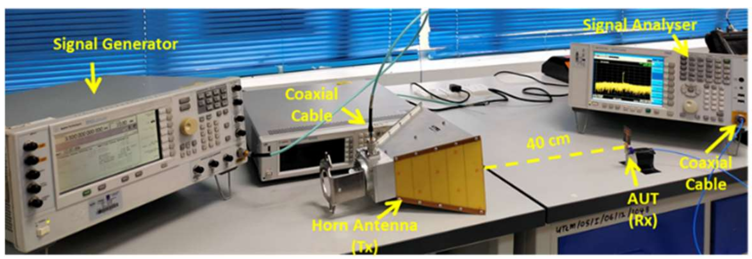

(e) LOS Measurement setup for SEA

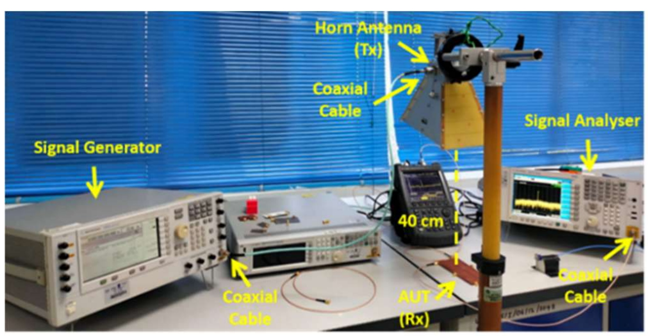

(f) LOS Measurement setup for MIMO

(g) On body bending setup

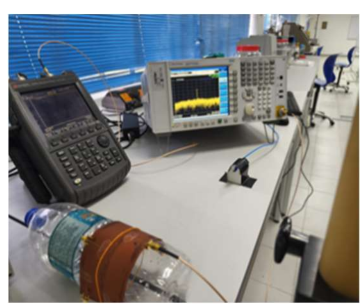

(e) Bending setup on bottle

Fig. 4 Different measurement setups for different validation scenarios

4. Results and Discussions

Figure 5 summarizes the simulated and also the measured performance of the proposed SEA. In particular, Figure 5 (a) compares the simulated reflection coefficients obtained throughout the five design stages over 2-8 GHz. The initial structure, S1, consists of a single circular radiator backed by a full ground plane and does not satisfy the −10dB impedance-matching criterion within the investigated range. Replacing the full ground with a partial ground plane in S2 introduces an operating band of approximately 4.0-6.5 GHz; however, the targeted 3.5 GHz frequency remains uncovered.

In S3, the addition of the defected ground structure extends the upper operating limit beyond 8 GHz, while the lower band edge remains near 4 GHz. The three-patch arrangement introduced in S4 slightly shifts the response but does not provide sufficient matching at 3.5 GHz. Finally, the five-circular-patch configuration in S5 improves the lower-frequency response considerably, producing a pronounced resonance of approximately −40dB near 3.5 GHz. Consequently, the optimized SEA achieves an approximate −10dB impedance bandwidth of 3.0-6.5 GHz.

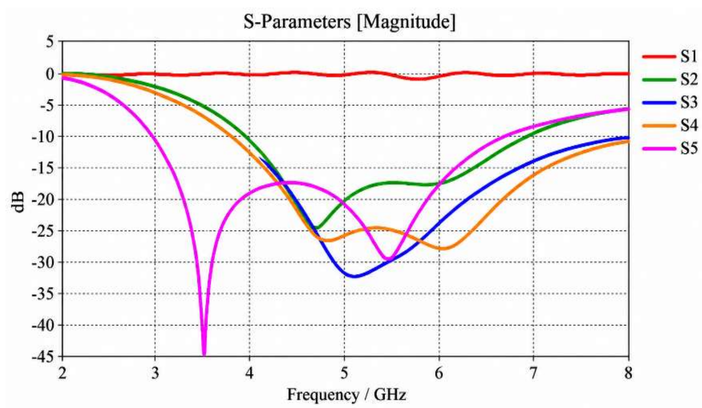

(a) S11 responses for different stages of the SEA design

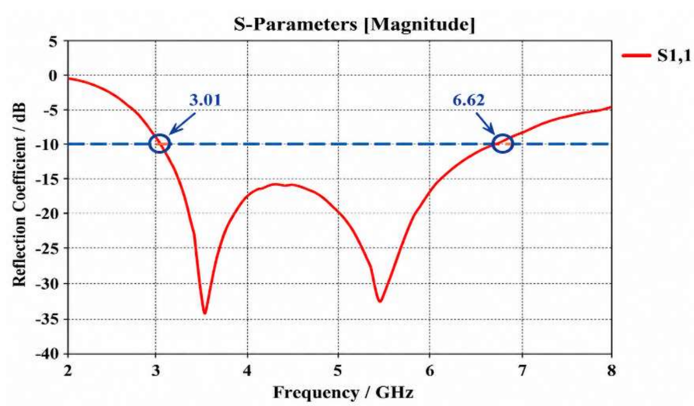

(b) Final simulated S11

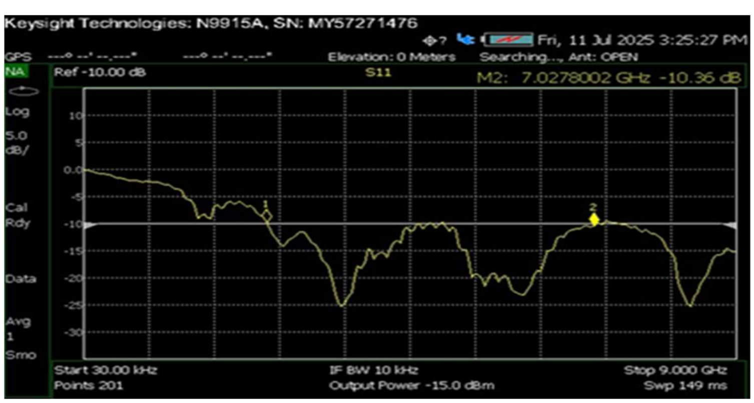

(c) Measured S11 from VNA

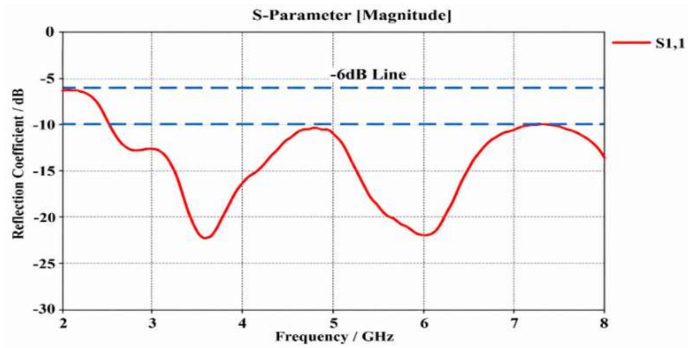

(d) Measured S11

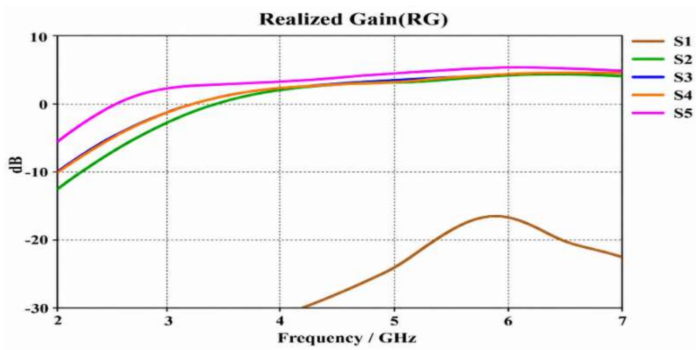

(e) The realize peak gain for each design steps

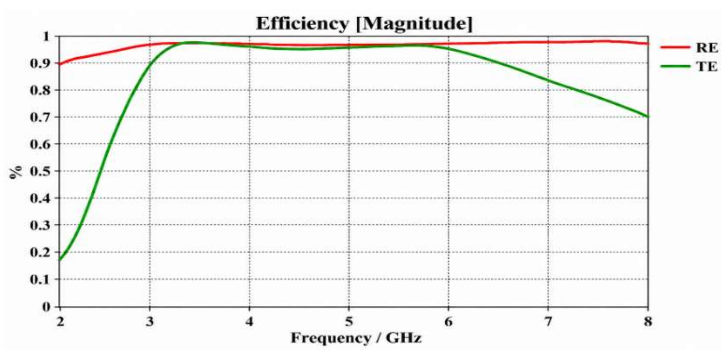

(f) Final RE and TE of the SEA

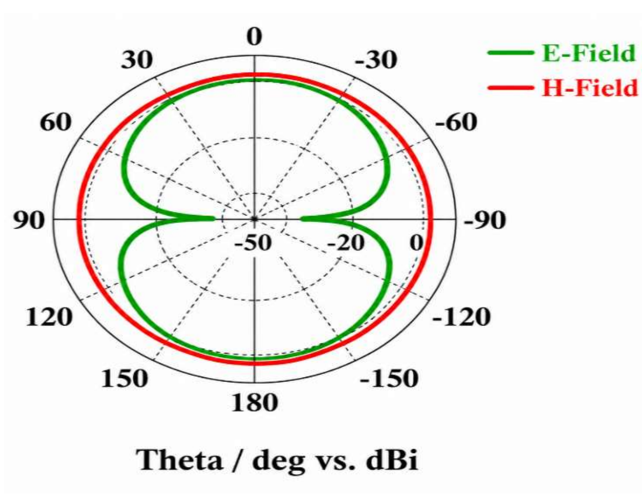

(g) Simulated far-field at 3.5 GHz

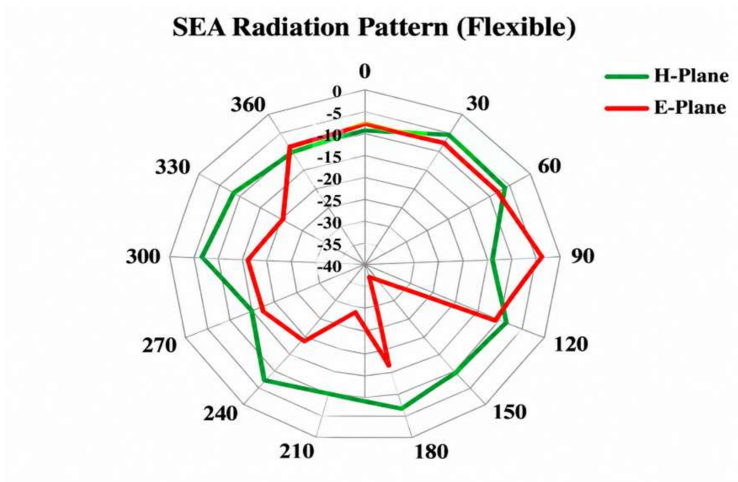

(h) Measured far-field at 3.5 GHz

Fig. 5 S-parameter and Far-field results for SEA

Figure 5 (c) and 5 (d) represent the measured S_{11} of the SEA. It is seen that the simulation and measured S_{11} maintain a good agreement in terms of the BW preservation. In both cases, the BW is acceptable within 3 - 6 GHz, whereby their slight deviation is observed. Those deviations may be due to the multi-step etching process, imperfect substrate material and SMA connector soldering. Similar to S_{11} improvement, in Figure 5 (e), the stage-by-stage gain enhancement is illustrated. It is seen that from stage 1, there is no gain at all, whereby finally at the last stage, the peak realized gain is at its highest, achieving 2.6 dBi at 3.5 GHz, and max around 4.8 dBi at 6.2 GHz. Figure 5 (f) discloses the RE and the TE of the proposed SEA. The RE remains consistently above 95%, while the TE stays mostly above 90% across the entire bandwidth. These results confirm that the proposed designs maintain a nice performance within the aimed operational working band. Lastly, Figure 5 (g) and Figure 5 (h) disclose the simulated and measured 2-D E- and H-plane radiation patterns of the SEA, respectively. From both results, it can be established that the antenna has an omni-directional pattern.

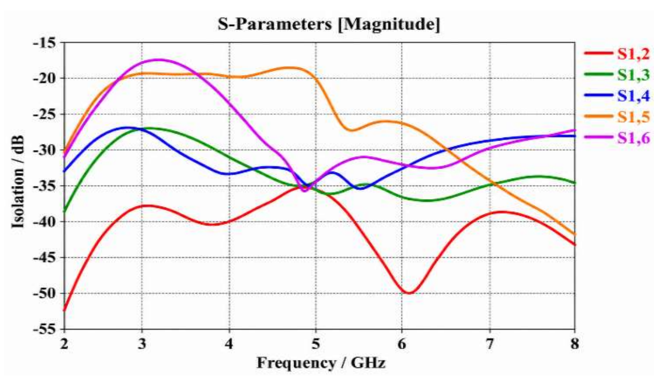

(a) Isolation for port 1 to other port (S)

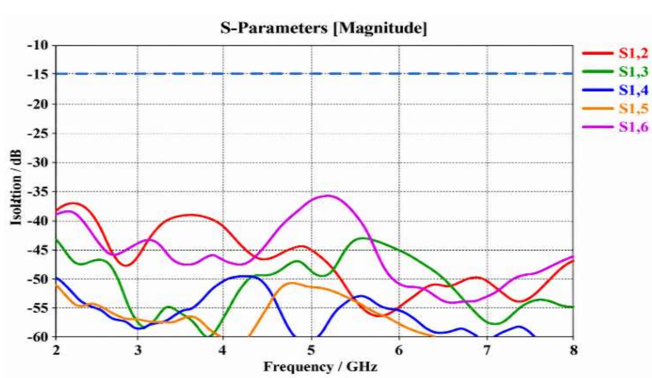

(b) Isolation for port 1 to other port (M)

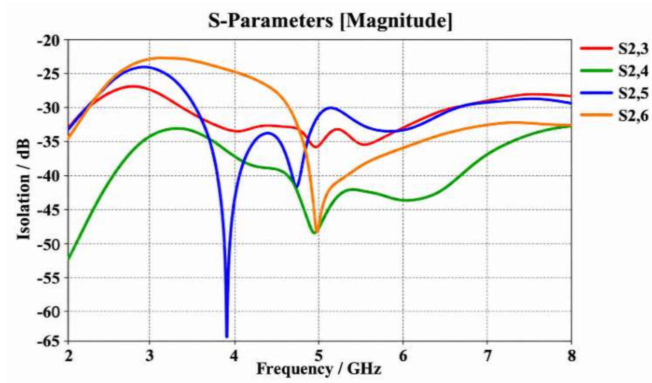

(c) Isolation for port 2 to other port (S)

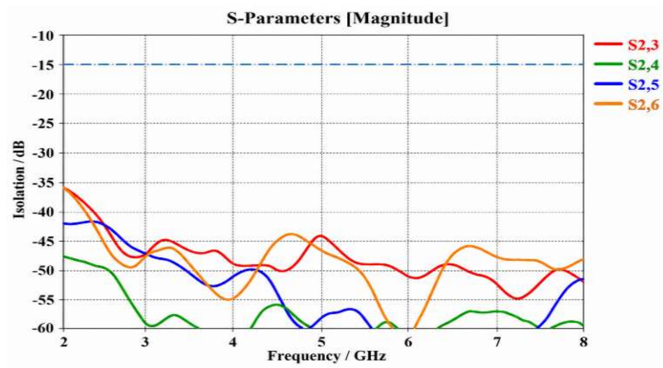

(d) Isolation for port 2 to other port (M)

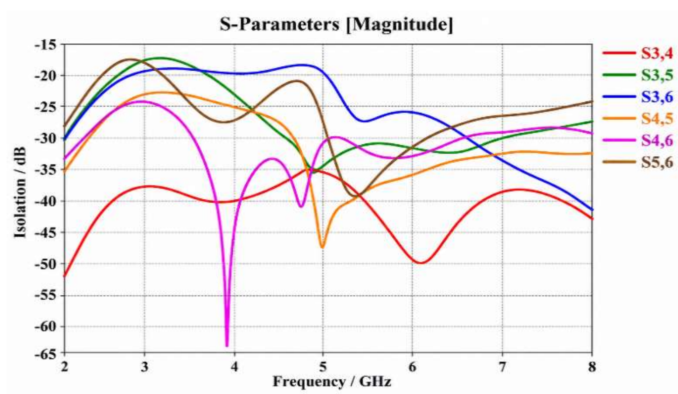

(e) Isolation for rest of the ports (S)

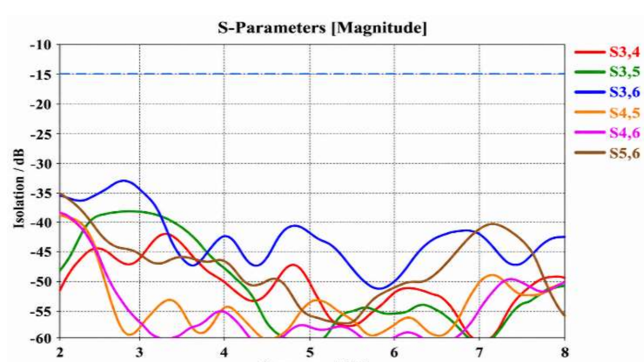

(f) Isolation for rest of the ports (M)

Fig. 6 Isolation results (a) Port 1 to other ports, (b) Port 2 to others, and (c) The rest ports of 6×6 MIMO.

Figure 6 comprises the port-to-port isolation simulation (S) and measured (M) results of the 6×6 MIMO configuration. It can be seen that the values are below -15dB across 2-8 GHz, with the best isolation for Figure 6 (a) near - 50dB, whereby for other ports shown in (c) and (e) around -65dB. Figures 6 (b), (d) and (f) present the measured isolation responses of the 6×6 MIMO antenna, covering all possible port combinations. Figure 6 (b) shows the isolation of Port 1 with respect to Ports 2-6, Figure 6 (d) shows the isolation of Port 2 with respect to Ports 3-6, and Figure 6 (f) illustrates the isolation among Ports 3-6. In all cases, the S-parameter pairs display nearly identical responses, confirming the reciprocity of the system.

The isolation values across the configuration range from a maximum (weakest isolation) of about -35.5 dB (S16) to a minimum (strongest isolation) of nearly -58 dB for certain port combinations such as S25 and S36. These results far exceed the -15 dB threshold typically required for MIMO systems, demonstrating excellent suppression of mutual coupling. Hence, the proposed 6×6 MIMO configuration ensures robust isolation performance across all ports, which is essential for reliable multi-port operation and high-capacity wireless communication. This indicates very low coupling and good isolation in 6×6 MIMO system.

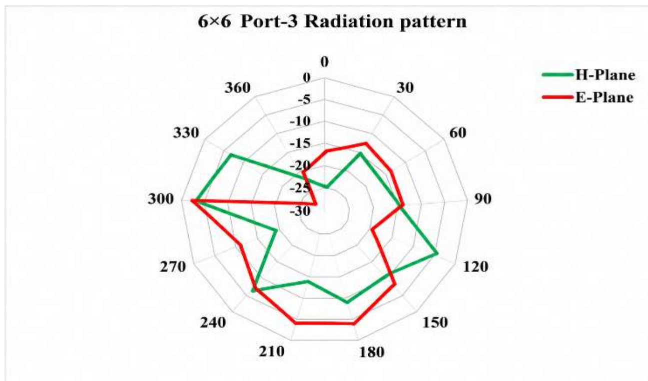

(a)

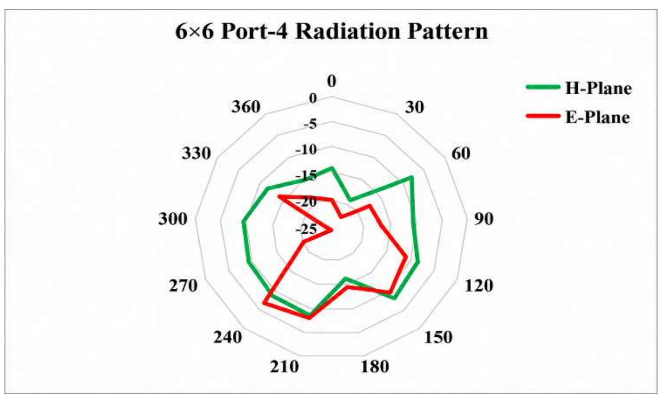

(b)

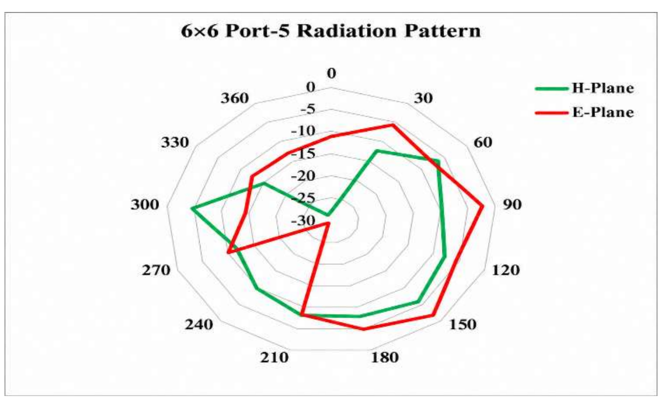

(c)

Fig. 7 Far field E- and H-plane pattern of the MIMO for, (a) Port 3, (b) Port 4, and (c) Port 6.

Furthermore, Figure 7 illustrates the measured 2D radiation patterns of the 6×6 MIMO configuration, where (a) corresponds to Port 3, (b) to Port 4, and (c) to Port 5. Only these three ports are shown, as the responses of the remaining ports are similar and exhibit the same radiation characteristics. Across all cases, the measured radiation patterns are observed to be nearly omnidirectional, with only minor deviations attributable to fabrication and measurement tolerances.

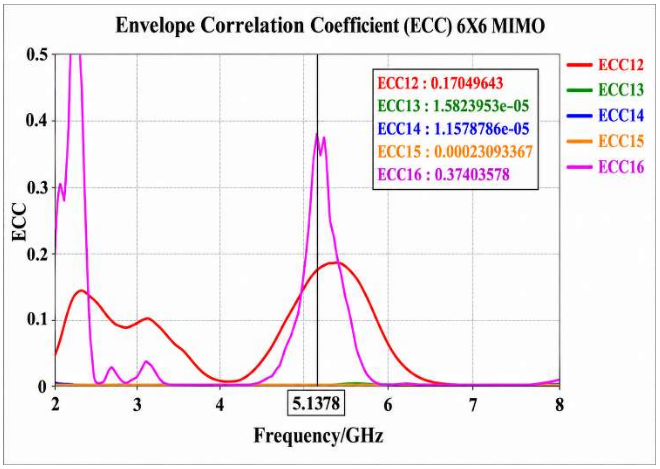

(a) ECC

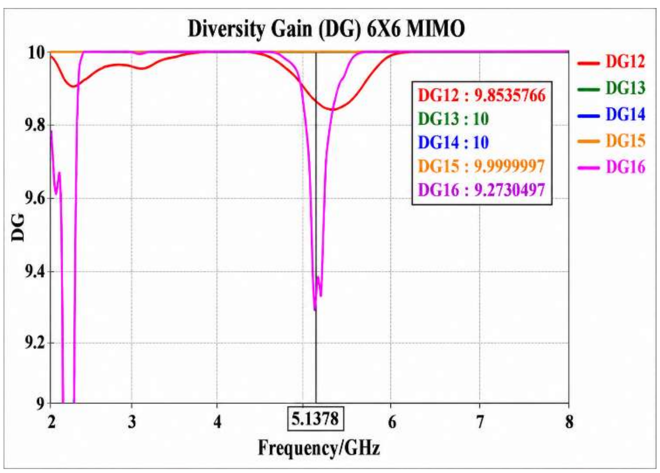

(b) DG

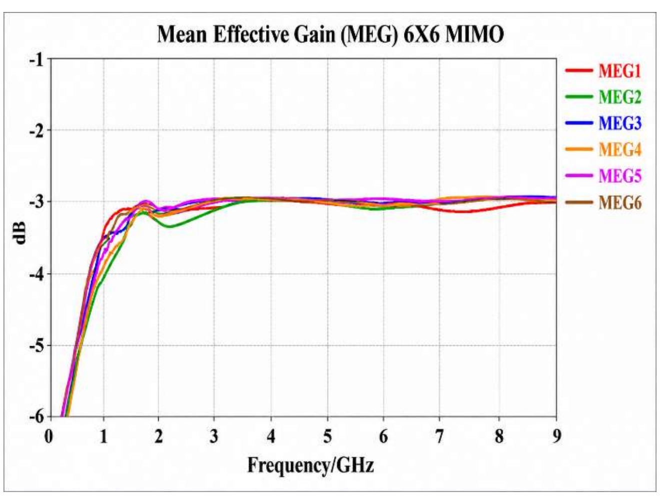

(c) Each port MEG

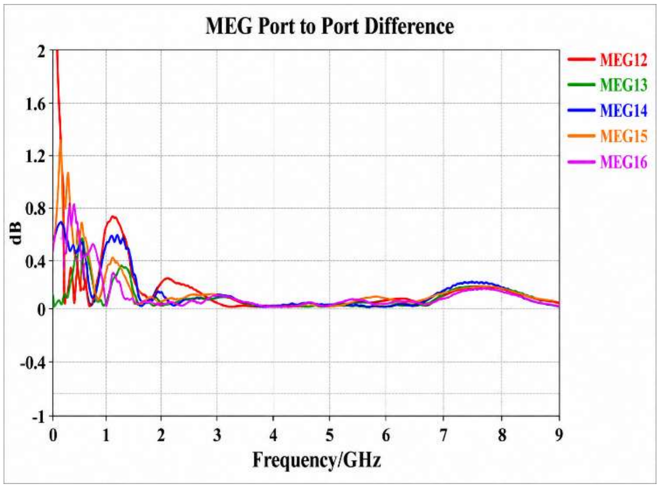

(d) MEG differences

Fig. 8 MIMO performance parameter responses

Moving onto MIMO parameters, Figure 8 (a) reveals the measured ECC values for the 6×6 MIMO configuration, where all port combinations (ECC12-ECC16) exhibit values well below 0.5. The lowest values are in the order of 1.15×10^{-5} (ECC14), while the highest remains at approximately 0.37, still within the acceptable limit. Figure 8 (b) illustrates the DG responses of the MIMO design. It is seen that all port combinations (DG12-DG16) consistently achieve values close to 10 dB. The lowest observed values are approximately 9.27 dB at ~ 5.14 GHz, while the highest are nearly 10 dB.

In terms of the MEG responses, Figure 8 (c) and Figure 8 (d) comprise the port-by-port MEG and MEG differences, respectively. It is observed that the MEG values for all six ports are nearly identical, averaging nominally around -3 dB, and the MEG differences between ports (MEG12-MEG16) remain close to 0 dB throughout the band. These results confirm that 6×6 MIMO systems provide excellent diversity performance with minimal correlation between antenna elements, ensuring reliable operation in the 3.5 GHz band.

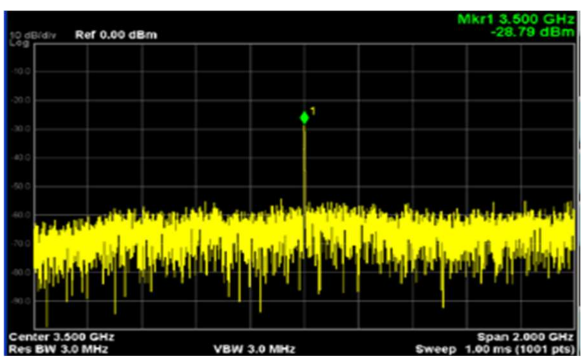

(a) SEA front

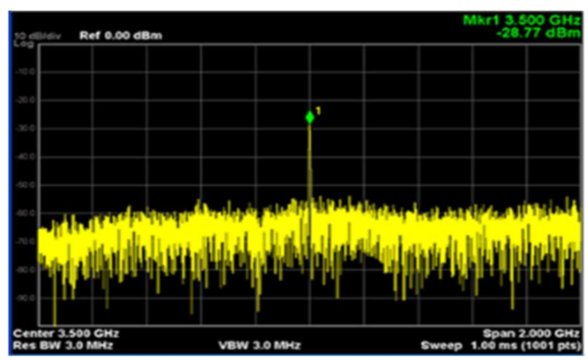

(b) SEA back

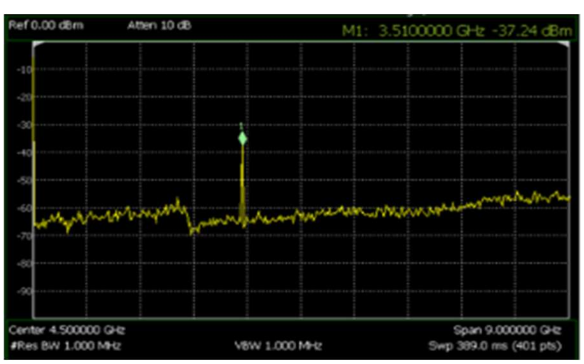

(c) Port 1

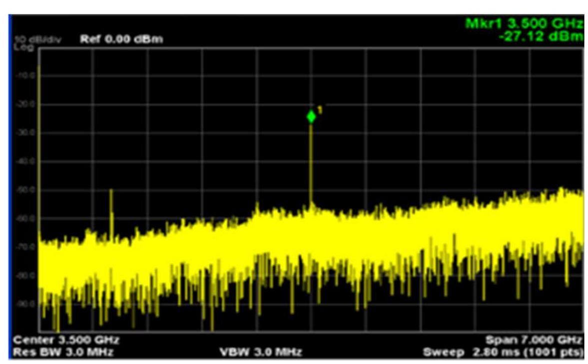

(d) Port 2

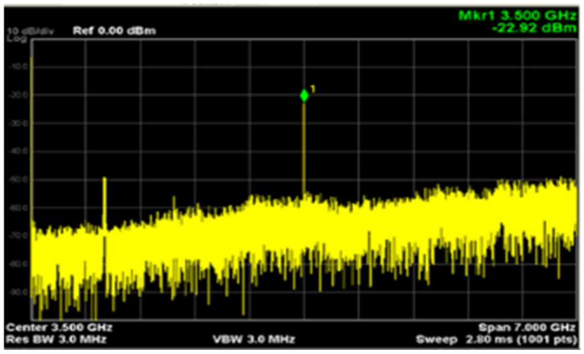

(e) Port 3

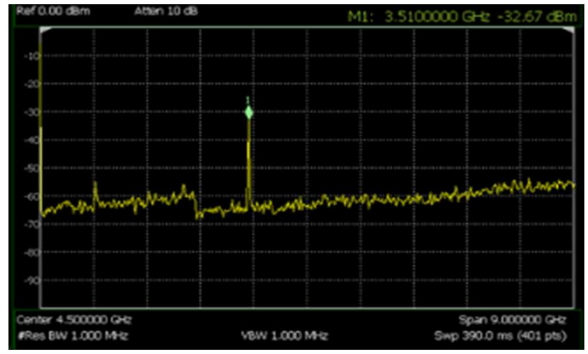

(f) Port 4

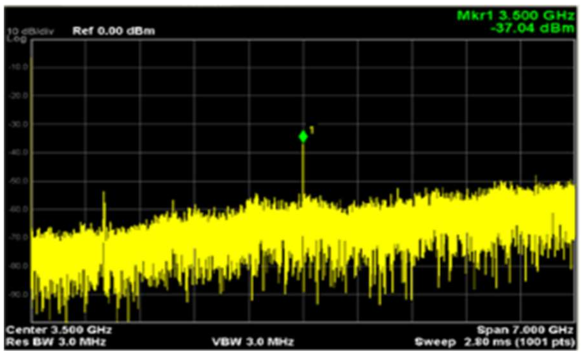

(g) Port 5

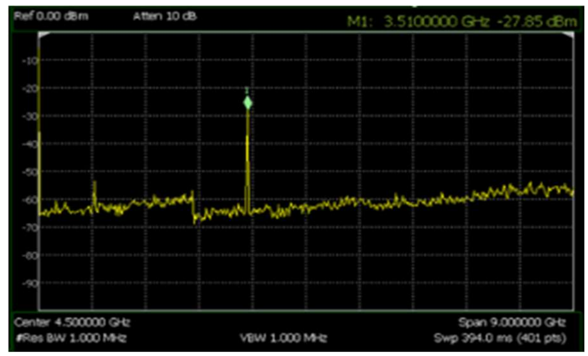

(h) Port 6

Fig. 9 Received power for LOS validation for SEA and MIMO designs

Figure 9 shows the LOS validation results for both SAE and MIMO designs. Figure 9 (a) and Figure 9 (b) LOS results for SEA (PCB) in both front and back orientations, where the received powers are measured at -28.77 dBm and -23.64 dBm, respectively. This demonstrates that the antenna radiates in both directions, with the back radiation being slightly stronger due to structural effects. Figure 9 (c) - Figure 9 (h) illustrates the LOS measurements for the 6×6 flexible MIMO configuration for Port 1 - Port 6, respectively. The received powers are -37.24 dBm (Port 1), -27.12 dBm (Port 2), -22.92 dBm (Port 3), -32.67 dBm (Port 6), -37.04 dBm (Port 4), and -27.85 dBm (Port 5). As expected, the variations across ports, such as those pairs, port 1 & 2, port 3 & 6 and port 4 & 5, are polarization-mismatched. All responses confirm consistent radiation and effective reception within the 3.5 GHz band. Overall, these LOS measurements validate the functionality of the SEA and the 6×6 MIMO prototypes, confirming their ability to sustain reliable communication links at the mid-band 5G frequency.

Figure 10 illustrates the received power, validating the functionality of the 6×6 flexible MIMO antenna under on-body and bending conditions at 3.5 GHz. When placed on the arm, the received power is -34.81 dBm (Figure 10 (a)). For bending scenarios, the received power is -34.18 dBm with a radius of 50 mm (Figure 10 (b)). These results confirm that the antenna maintains reliable performance across different deformation and on-body conditions: deformations and body-loading effects.

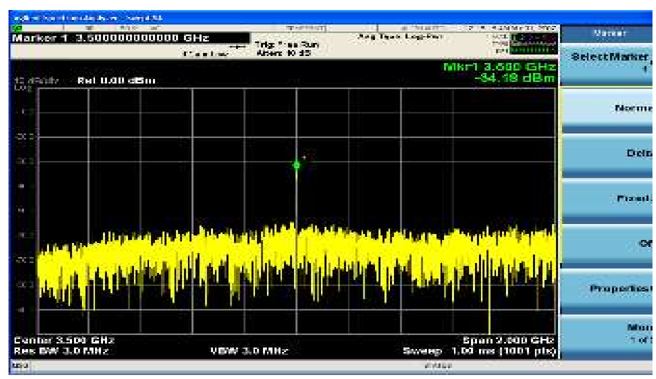

(a)

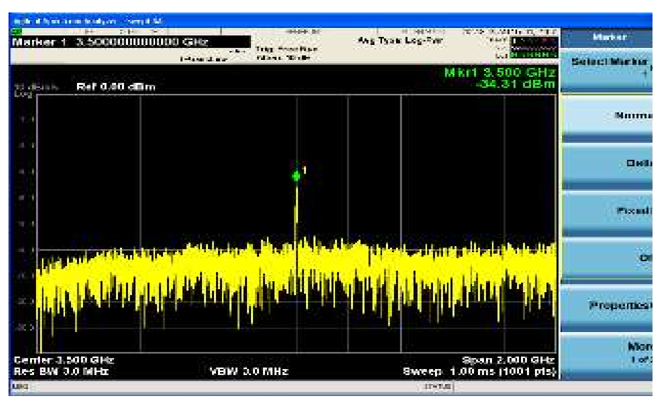

(b)

Fig. 10 LOS validation for, (a) On body, and (b) Bending with 50mm radius bottle bending conditions.

Figure 11 shows the setup for the SAR calculation in CST MWS. Table 2 comprises the calculated values at 3.5 GHz. The SAR table presents the radiation absorption levels of a 6×6 MIMO antenna system when each port is individually activated near a head model. The SAR values are given for both 1g and 10g tissue averaging, representing localized and broader absorption, respectively. Among all ports, Port 4 exhibits the highest SAR with 0.775 W/kg (1g) and Port 6 exhibits 0.335 W/kg (10g), indicating a stronger interaction with the head tissue, possibly due to its position or radiation pattern. In contrast, Port 1 shows the lowest SAR values (0.287 W/kg for 1g and 0.119 W/kg for 10g), suggesting better safety performance. All values remain within internationally accepted safety limits (1.6 W/kg for 1g and 2.0 W/kg for 10g), confirming the antenna's compliance with exposure standards.

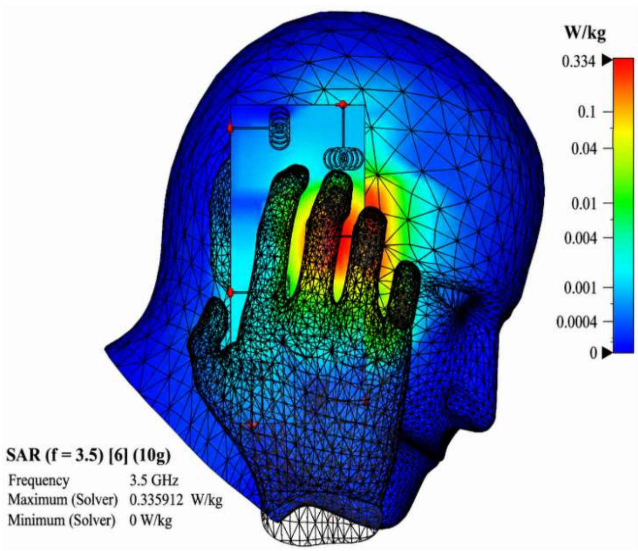

Fig. 11 SAR calculation setup in CST MWS

From all the results presented, it can be seen that the isolation and bandwidth reported above exceed what Table 1 records for comparable sub-6 GHz arrays, and three aspects of the design account for the difference. Most handset MIMO arrays position their elements along the edges of a single continuous ground plane, which leaves the ground itself as the dominant coupling path.

The ground used here removes that path, since each radiator sits above its own partial ground rather than a shared conductor. The defected ground structure then interrupts the residual current near the feed region, which is where coupling concentrates once the ground has been truncated. Neighbouring elements are additionally rotated by 90°, so whatever energy does couple arrives in the orthogonal polarization and contributes little to the transmission between ports. The wide continuous band originates from a separate mechanism: the five circular patches resonate at closely spaced frequencies, and the partial ground broadens each resonance sufficiently for them to merge into a single 3.0-6.6 GHz response rather than the two narrow sub-bands characteristic of the dual-band designs in [13, 17]. The comparison is not entirely like-for-like, and this should be stated plainly.

Table 2. SAR results for 6×6 MIMO

Ports	1g (W/Kg)	10g (W/Kg)
1-Port	0.287	0.119
2-Port	0.614	0.182
3-Port	0.357	0.116
4-port	0.775	0.149
5-Port	0.585	0.143
6-Port	0.303	0.335

The arrays in Table 1 fit eight or ten elements into a handset chassis at spacings of roughly 10-25 mm, whereas the present design uses six elements with 84 mm between the most widely separated pairs, so part of the isolation advantage follows from the larger separation that a lower element count permits. The design is therefore best understood as trading MIMO order for isolation, bandwidth and mechanical flexibility, a trade that suits wearable and biomedical terminals where element count matters less than link robustness under bending and on-body loading.

5. Conclusion

This study introduces a planar 6-element MIMO antenna realized on flexible substrate Kapton NH for sub-6 GHz 5G wireless communication systems. This proposed design associates a multi-circular radiator with a PGP and a DGS to improve the impedance matching, expand the operating bandwidth, reduce inter-element mutual coupling, and further improves the diversity characteristics of the MIMO configuration. This optimized design achieved a wideband operation from 3.0 to 6.6 GHz, covering important sub-6 GHz 5G all mid bands. The simulated and the measured results showed good agreement, authenticating the reliability of the proposed SEA and MIMO design. The fabricated 6×6 MIMO antenna demonstrated very good mutual coupling reduction, with measured isolation reaching as > -35 dB across the operating band. The antenna also achieved very low ECC values of 0.000015, nearly 10 dB diversity gain, stable MEG performance around -3dB, and nearly omnidirectional radiation characteristics, demonstrating a strong suitability for high-capacity MIMO communication in 5G.

In addition to that, the LOS measurements validated the practical communication capability of the antenna further, while the bending and the on-body tests confirmed its flexibility and stable operation under realistic conditions. Furthermore, the SAR analysis additionally confirmed that all ports remain within internationally accepted safety limits, with a maximum 1 g SAR of 0.775 W/kg and a maximum 10 g SAR of 0.335 W/kg. Overall, the proposed flexible six-element MIMO antenna exhibits a wide bandwidth, a high isolation, low correlation, safe SAR radiation performance, and practical validation, making it well capable design for wearable devices, compact 5G smartphones and other available flexible biomedical and wireless in 5G mid band spectrum.

Conflicts of Interest

The authors declare that there is no conflict of interest regarding the publication of this paper.

Funding Statement

This research is funded by the funded by the Center for Research and Innovation Management (CRIM), Universiti Teknikal Malaysia Melaka (UTeM), with the Short-Term Grant Scheme (PJP) with grant No. PJP/2024/FTKEK/PERINTIS/SA0017.

Acknowledgments

All Authors have contributed equally to this work.

References

[1] Mohamed M. Morsy, "Compact Eight-Element MIMO Antenna Array for sub 6 GHz Mobile Applications," *SN Applied Sciences*, vol. 5, no. 10, pp. 1-7, 2023. [CrossRef] [Google Scholar] [Publisher Link]

[2] Muhammad Zahid et al., "Ten-Port MIMO Inverted-F Antenna for LTE Bands 43/48/49 Bands Smartphone Applications," *Electronics*, vol. 12, no. 19, pp. 1-14, 2023. [CrossRef] [Google Scholar] [Publisher Link]

[3] Chih-Chung Lin et al., "Compact Sub 6 GHz Dual Band Twelve-Element MIMO Antenna for 5G Metal-Rimmed Smartphone Applications," *Micromachines*, vol. 14, no. 7, pp. 1-17, 2023. [CrossRef] [Google Scholar] [Publisher Link]

[4] Zhonggen Wang et al., "Design of MIMO Antenna with Double L-Shaped Structure for 5G NR," *Symmetry*, vol. 15, no. 3, pp. 1-13, 2023. [CrossRef] [Google Scholar] [Publisher Link]

[5] Zhouyou Ren, and Anping Zhao, "Dual-Band MIMO Antenna with Compact Self-Decoupled Antenna Pairs for 5G Mobile Applications," *IEEE Access*, vol. 7, pp. 82288-82296, 2019. [CrossRef] [Google Scholar] [Publisher Link]

[6] Jiangwei Sui et al., "A Dual-Band Decoupling Technique for MIMO Antenna Systems using Composite Capacitor Circuits," *IEEE Transactions on Circuits and Systems II: Express Briefs*, vol. 71, no. 1, pp. 116-120, 2024. [CrossRef] [Google Scholar] [Publisher Link]

[7] Mohammad S. Sharawi, "Printed Multi-Band MIMO Antenna Systems and their Performance Metrics [Wireless Corner]," *IEEE Antennas and Propagation Magazine*, vol. 55, no. 5, pp. 218-232, 2013. [CrossRef] [Google Scholar] [Publisher Link]

[8] Zhan Xu, and Changjiang Deng, "High-Isolated MIMO Antenna Design based on Pattern Diversity for 5G Mobile Terminals," *IEEE Antennas and Wireless Propagation Letters*, vol. 19, no. 3, pp. 467-471, 2020. [CrossRef] [Google Scholar] [Publisher Link]

[9] Aidi Ren et al., "A Broadband MIMO Antenna based on Multimodes for 5G Smartphone Applications," *IEEE Antennas and Wireless Propagation Letters*, vol. 22, no. 7, pp. 1642-1646, 2023. [CrossRef] [Google Scholar] [Publisher Link]

[10] Yong Qiang Hei, Jia Geng He, and Wen Tao Li, "Wideband Decoupled 8-Element MIMO Antenna for 5G Mobile Terminal Applications," *IEEE Antennas and Wireless Propagation Letters*, vol. 20, no. 8, pp. 1448-1452, 2021. [CrossRef] [Google Scholar] [Publisher Link]

[11] Jianlin Huang et al., "A Quad-Port Dual-Band MIMO Antenna Array for 5G Smartphone Applications," *Electronics*, vol. 10, no. 5, pp. 1-9, 2021. [CrossRef] [Google Scholar] [Publisher Link]

[12] Umair Rafique et al., "Uni-Planar MIMO Antenna for Sub-6 GHz 5G Mobile Phone Applications," *2022 IEEE Wireless Antenna and Microwave Symposium (WAMS)*, Rourkela, India, pp. 1-5, 2022. [CrossRef] [Google Scholar] [Publisher Link]

[13] Saqer S. Alja'afreh et al., "Ten Antenna Array using a Small Footprint Capacitive-Coupled-Shorted Loop Antenna for 3.5 GHz 5G Smartphone Applications," *IEEE Access*, vol. 9, pp. 33796-33810, 2021. [CrossRef] [Google Scholar] [Publisher Link]

[14] Yu-Tung Chen, and Hsin-Lung Su, "A Sub-6 GHz 8 × 8 MIMO Antenna Array for 5G Metal-Frame Mobile Phone Applications," *Electronics*, vol. 13, no. 23, pp. 1-16, 2024. [CrossRef] [Google Scholar] [Publisher Link]

[15] Deepthi Mariam John et al., "Characteristics mode Analysis based Wideband Sub-6 GHz Flexible MIMO Antenna using a Unique Hybrid Decoupling Structure for Wearable Applications," *Physica Scripta*, vol. 99, no. 3, pp. 1-29, 2024. [CrossRef] [Google Scholar] [Publisher Link]

[16] Pendli Pradeep et al., "Development of Wearable Textile MIMO Antenna for Sub-6 GHz Band New Radio 5G Applications," *Micromachines*, vol. 15, no. 5, pp. 1-14, 2024. [CrossRef] [Google Scholar] [Publisher Link]

[17] Antony Judice, Shivani Malhotra, and Manish Sharma, "Micromachined Octa-Port High Self Isolation Asymmetric Tapered Feed MIMO Antenna with Flexible Capabilities and SAR Analysis Integrating 5G-Sub 6 Ghz, Microwave, and Millimeter-Wave Applications," *Wireless Networks*, vol. 31, no. 4, pp. 3365-3394, 2025. [CrossRef] [Google Scholar] [Publisher Link]

[18] Vandana Yadav et al., "Dual and Wideband 6-port MIMO Antenna for WiFi, LTE and Carrier Aggregation Systems Applications," *AEU - International Journal of Electronics and Communications*, vol. 162, 2023. [CrossRef] [Google Scholar] [Publisher Link]

[19] Jingli Guo et al., "Side-Edge Frame Printed Eight-Port Dual-Band Antenna Array for 5G Smartphone Applications," *IEEE Transactions on Antennas and Propagation*, vol. 66, no. 12, pp. 7412-7417, 2018. [CrossRef] [Google Scholar] [Publisher Link]